nature materials

Article

https://doi.org/10.1038/s41563-026-02613-7

Ultralow-voltage electrochemical organic light-emitting transistors with pinned and wide lateral recombination

Received: 7 March 2025

Accepted: 20 April 2026

Published online: 08 June 2026

Check for updates

Kwan-Nyeong Kim[1,7], Huanyu Zhou[1,7], Dong-Yoon Kim[1], Min-Jun Sung[1], Woo Jin Jeong[1], Dae-Gyo Seo[1], Jinwoo Park[1], Seungbeom Lee[2], Yilei Wu[3], Yeongjun Lee[3], Kyun Kyu Kim[3], Jaeho Park[3], Yanxiang Cheng[4], Hea-Lim Park[2], Zhenan Bao[3] & Tae-Woo Lee[1,5,6]

Light emission from organic transistors holds strong potential for user-interactive functionality across applications ranging from wearable and biointegrated systems to neuromorphic electronics. However, conventional single-active-layer organic transistors suffer from inefficient charge carrier injection, resulting in high drain voltages (>80 V in field-effect devices and >3.5 V in electrochemical devices with p–i–n junctions) and narrow, spatially dynamic recombination zones (<75 μm). Here we report a single-active-layer electrochemical organic light-emitting transistor with drain-side electric double layer formation, achieving ultralow-voltage operation (<3.5 V) together with a wide, spatially pinned recombination zone. An ion transport enhancer in the light-emitting polymer channel induces an electric double layer at the drain electrode, overcoming limited electron injection without n-type doping. This mechanism enables flexible, large-area devices with a recombination zone width of 267 μm and a maximum luminance of 826 cd m^{-2} at 3.5 V, and operation with two 1.5-V batteries. This work advances single-active-layer OLETs and paves the way for organic electronic systems with intuitive, user-friendly visualization functions.

Organic electronic devices are increasingly being developed to enable user-friendly systems that can interface with the human body, process biosignals and provide direct feedback within a single platform. In this context, organic transistors are attractive electronic building blocks for wearable and biointegrated systems in which soft form factors and low-voltage operation are essential[1–8]. Beyond conventional switching, organic transistors exhibiting threshold behaviour and analogue memory enable neuromorphic systems for bio-hybrid artificial nerves, neuro-inspired soft robots and neuromorphic computing[9–12]. Despite this promise, a critical challenge remains in presenting processed signals in a direct visual form, which is essential for users to immediately perceive real-time system feedback. Integrating such visualization functionality without introducing other devices and preserving the simplicity of the transistor architecture, therefore, represents a compelling direction for interactive electronic systems using organic transistors.

[1]Department of Materials Science and Engineering, Seoul National University, Seoul, Republic of Korea. [2]Department of Materials Science and Engineering, Seoul National University of Science and Technology, Seoul, Republic of Korea. [3]Department of Chemical Engineering, Stanford University, Stanford, CA, USA. [4]State Key Laboratory of Polymer Physics and Chemistry, Changchun Institute of Applied Chemistry, Chinese Academy of Sciences, Changchun, People's Republic of China. [5]Interdisciplinary Program in Bioengineering, Institute of Engineering Research, Research Institute of Advanced Materials, Seoul, Republic of Korea. [6]SN Display Co. Ltd, Seoul, Republic of Korea. [7]These authors contributed equally: Kwan-Nyeong Kim, Huanyu Zhou. e-mail: twlees@snu.ac.kr

https://doi.org/10.1038/s41563-026-02613-7

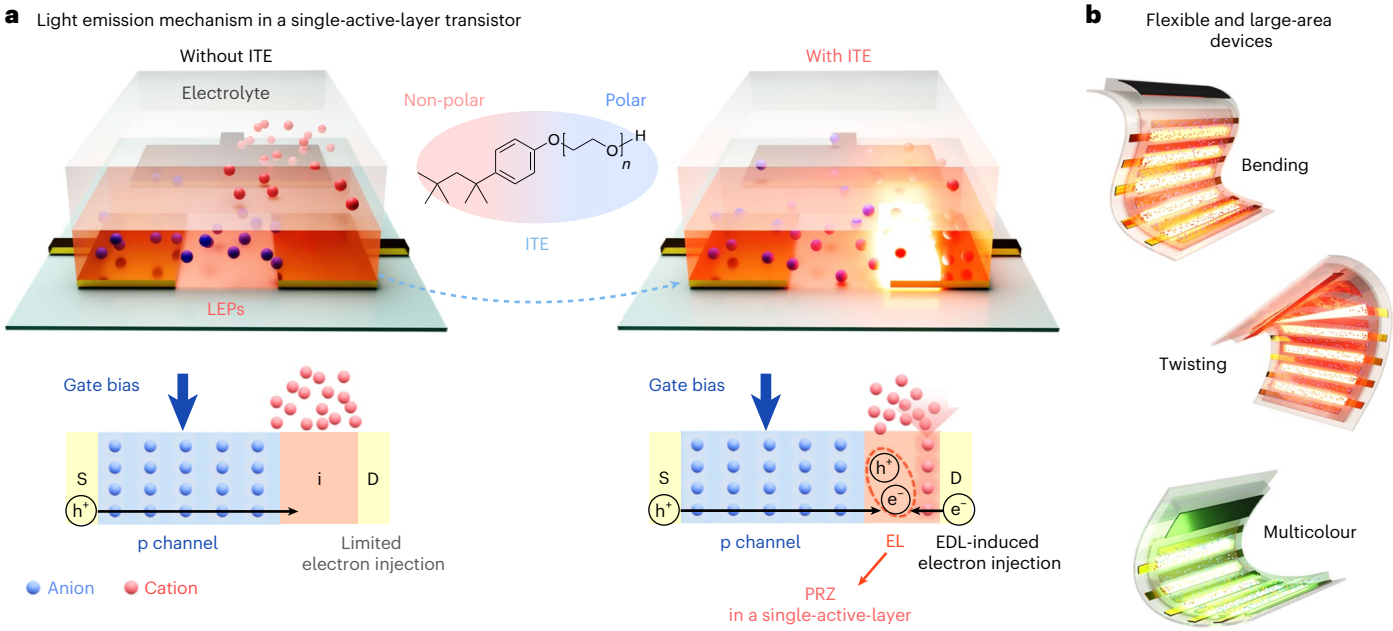

Fig. 1 | Design of a single-active-layer EOLET. a, In conventional electrolyte-gated transistor with an LEP channel, electrolyte gating can induce hole transport through the p-channel induced by the electrochemical anion doping of the LEP, but electron injection is absent; therefore, charge carrier recombination is very limited even when LEPs are used as channels. Introducing ITE into the LEP channel facilitates ion transport and forms the cation EDL at the LEP/drain electrode interface. This improves electron injection at even lower voltage than the energy-gap potential ($|V_{DS}| < |E_g/e|$) and forms a PRZ. **b**, Schematics of flexible and large-area emission in EOLET. The EDL-induced electron injection allows large-area light emission in the p-channel organic transistor. In addition, the flexible nature of LEP enables mechanical flexibility of EOLET suitable for on-skin applications.

To achieve such functional integration, organic light-emitting materials can be directly used as the transistor channel to form organic light-emitting transistors (OLETs), which preserve a simple transistor geometry and enable light emission[13–20]. However, in conventional field-effect OLETs, inefficient charge injection from metal electrodes into the channel necessitates high drain voltages, typically exceeding 80 V, and results in narrow and spatially dynamic recombination zones with widths below 45 µm (refs. 13–16). Electrochemical OLETs (EOLETs), which use electrolytes as dielectric layers, can reduce operating voltages to approximately 3.5–5 V by exploiting high interfacial capacitance and electrochemical doping of the channel. Nevertheless, their light emission originates from electrochemically induced dynamic p–i–n junction formation in the channel, and the propagation of ionic doping fronts even without gate voltage leads to spatially unstable and narrow recombination zones (<75 µm)[17–20]. This intrinsic instability of the recombination profile fundamentally limits controllable light emission. Despite the conceptual simplicity of transistor architectures, achieving the multifunctionality of neuromorphic processing and light emission capability with a low operating voltage has remained a long-standing fundamental challenge.

Here we present a single-active-layer electrochemical organic light-emitting transistor (EOLET) that enables ultralow-voltage operation (<3.5 V) together with a wide and spatially pinned recombination zone (PRZ). This behaviour is achieved by incorporating an ion transport enhancer (ITE) into a single light-emitting polymer (LEP) channel layer, which facilitates controlled ionic transport without introducing additional charge injection or transport layers. The enhanced ionic mobility induces the formation of electric double layers (EDLs) at the LEP/drain electrode interface under bias, thereby overcoming the intrinsic electron injection barrier and preventing the formation of ion-induced n-type doping fronts (Fig. 1a and Supplementary Fig. 1). As a result, light emission occurs at drain voltages ($|V_{DS}|$) lower than the bandgap potential (E_g) of the LEP ($|V_{DS}| < |E_g/e|$), and a non-moving PRZ is formed irrespective of gate voltage. Using this strategy, the EOLET achieves an unprecedented recombination zone width (RZW) of up to 267 µm with a maximum luminance of 826 cd m^{-2} at 3.5 V, and maintaining mechanical flexibility (Fig. 1b). Finally, we demonstrate wearable display systems powered by two 1.5-V batteries, highlighting their suitability as stand-alone platforms for wearable systems that directly visualize electronic signal processing.

Improving ion transport of LEP channel by ITE incorporation

We examined how ITE affected the structure and morphology of the LEP poly[2-methoxy-5-(2-ethylhexyloxy)-1,4-phenylenevinylene] (MEH-PPV) by controlling the ITE weight ratio (Methods).

Morphological changes in MEH-PPV films after introducing ITE were first evaluated using atomic force microscopy (AFM). Following ITE incorporation, a fibrillar structure developed (Supplementary Fig. 2). The non-polar group of ITE is interfaced with a non-polar alkyl side chain of MEH-PPV, and the polar groups are interfaced with each other, resulting in phase separation between the polar and non-polar groups[21]. This separation induces morphological shifts from coiled to linear chain conformations and may increase the persistence length of the polymer chain (Supplementary Fig. 3)[21].

The effect of ITE on the microstructure of the MEH-PPV was further quantified using grazing-incidence X-ray diffraction (GIXD) (Fig. 2a,b and Supplementary Table 1). The two-dimensional GIXD profile revealed that the MEH-PPV film is amorphous and contains crystallites that are oriented face-on along the out-of-plane direction (Fig. 2a)[22]. With the addition of ITE, the (010) π–π spacing increases slightly from 3.94 to 4.03 Å, whereas the in-plane (100) lamella stacking distance expands substantially from 16.75 to 21.65 Å. Given that nanofibril structure was observed in MEH-PPV with the ITE film, this substantial change in lamella stacking distance indicates that the ITE molecules predominantly reside near the alkyl side chain, causing a conformational transition of the LEP from a coiled to a linear structure.

Photoluminescence (PL) properties of MEH-PPV were evaluated with varying ITE content to further analyse the effect of structural

https://doi.org/10.1038/s41563-026-02613-7

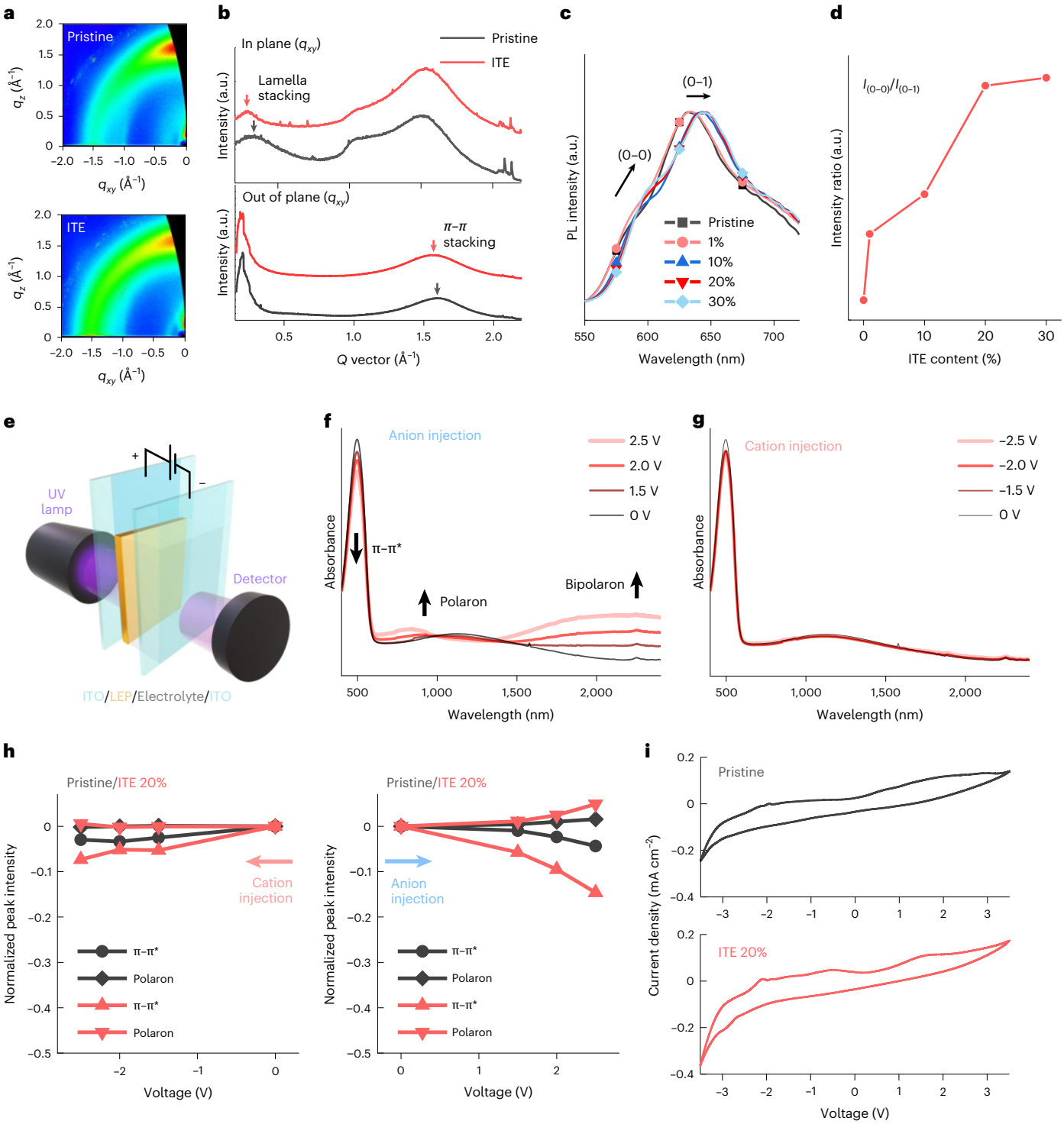

Fig. 2 | Improving ion transport of LEP channel by ITE incorporation. **a**,**b**, GIXD two-dimensional patterns (**a**) and one-dimensional diffractograms (**b**) of pristine MEH-PPV and ITE-incorporated MEH-PPV. **c**,**d**, PL spectra of LEP films according to the ITE contents and intensity ratio of $I_{(0-0)}$ and $I_{(0-1)}$ calculated from the PL spectra. **e**, Schematics of in situ UV–vis spectroscopy setup. **f**,**g**, Transition in the absorbance spectrum on voltage application. **h**, Normalized peak intensity of the absorbance spectrum as a function of doping voltage. **i**, Cyclic voltammetry curves of pristine and 20% ITE films.

changes. In the PL spectra, the 0–0 vibronic band near 590 nm corresponds to intrachain emission, whereas the 0–1 vibronic band near 630 nm corresponds to interchain emission[23,24] (Fig. 2c and Supplementary Fig. 4). By ITE blending, both peaks gradually redshifted, indicating an increase in the π-conjugation length in a fibrillar structure (Fig. 2c)[23,24]. This result aligns with structural analysis using AFM and GIXD. Furthermore, the ratio of the intensity I_{0-0} of the 0–0 band to the intensity I_{0-1} of the 0–1 band increased as the ITE content increased; this change implies an increase in intrachain emission compared with interchain emission, and occurs because the increase in ITE content causes the expansion of lamella (Fig. 2d)[23,24]. We further evaluated the effects of increasing the ITE content on the absorbance spectra and Tauc plots with varying ITE contents (Supplementary Fig. 5). The redshifts in the 0–0 peak near 500 nm and the decrease in E_g were

observed as the ITE content increased. This result also indicates that the overall π conjugation of the LEP film increases through ITE blending.

The influence of ITE on ion transport in the LEP, depending on the type of doping ions, was evaluated using an in situ ultraviolet visible (UV–vis) spectroscopy setup, and the electrolyte and MEH-PPV with the ITE films were sandwiched between two transparent ITO electrodes (Fig. 2e). On voltage application, ions drift from the electrolyte into the LEP film and induce the electrochemical doping of MEH-PPV, generating polaron and bipolaron states that appear as absorption peaks near 800 and 2,000 nm, respectively, instead of the neutral-state peak near 500 nm, simultaneously driving a benzoid-to-quinoid conformational transition that reduces the bandgap (E_g)[25]. This change results in the bleaching of the absorbance spectrum in the neutral states (Fig. 2f,g). To monitor this absorbance transition, we applied doping voltages from −2.5 V to 2.5 V for 30 s to the electrolyte film (Fig. 2f–h and Supplementary Fig. 6). On anion injection under a positive voltage, the absorbance intensity of the neutral state decreases as the applied voltage increases, whereas the intensities of polaron and bipolaron states increase. By contrast, during cation injections by negative voltages, only slight changes in the neutral state were observed, and the polaron formation was hardly detected. This indicates that n-type doping by $EMIM^+$ is more restricted than p-type doping by $TFSI^-$ in p-type-dominant MEH-PPV, this assymetry is a crucial factor for stable cationic EDL formation in device operation. Additionally, consistent with the observed absorbance transition results, cation injection induced significantly fewer charges than anion injections, indicating the more restricted electrochemical doping of MEH-PPV by $EMIM^+$ cations compared with $TFSI^-$ anions (Supplementary Fig. 7)[26]. This inherent asymmetry in doping efficiency within the LEP can be a critical characteristic that suppresses n-type doping and promotes cation transport, thereby enabling more stable and efficient electron injection in device operation.

We further evaluated the influence of ITE on the electrochemical doping rate in LEP as a function of the ITE content (Supplementary Fig. 8). As the ITE content increased from 0% to 10%, 20% and 30%, the rate of this absorbance transition increases, confirming that ion transport within the LEP film without ITE is highly restricted. This facilitation of ion transport was also confirmed by cyclic voltammetry results in which the addition of ITE led to an increased current density and the clear appearance of oxidation and reduction peaks (Fig. 2i)[27,28]. Therefore, ITE blending emerges as a promising strategy for enhancing ion transport and accelerating the electrochemical doping rate in LEP.

Operating mechanisms of EOLETs with drain-side EDL

To elucidate the operating mechanism of EOLET, we fabricated top-emitting p-channel organic transistor with bottom-contact and lateral-gated transistor architecture (Fig. 3a and Supplementary Figs. 9 and 10). Effective light emission requires efficient hole and electron injection from both source and drain electrodes, respectively. The hole injection barrier can be compensated by p-type doping in p-channel organic transistors[29,30]; therefore, the primary bottleneck for light emission is electron injection from the drain electrode.

To directly visualize the mechanism of recombination zone formation and transistor operation, in situ optical microscopy was measured with constant $V_{DS} = -2.50$ V by varying V_{GS}. In our strategy, cation-induced EDLs at the interface between the ITE-incorporated LEP (ITE-LEP) channel and the drain electrode facilitate electron injection without n-type doping. By controlling spontaneous cation migration into the channel in the OFF state ($V_{DS} < 0$ V, $V_{GS} = 0$ V) (Extended Data Fig. 1), the application of a negative gate bias in the ON state ($V_{DS} < 0$ V, $V_{GS} < 0$ V) forms a p-channel from the source to the drain without n-type doping near the drain, thereby pinning the recombination zone without the propagation of doping fronts, unlike conventional dynamic p–i–n junction formation (Supplementary Figs. 1 and 11)[17].

The electroluminescence (EL) properties of EOLET were further measured by forward and subsequent backward sweeps from $V_{DS} = 0$ V to −2.5 V with fixed $V_{GS} = -1.0$ V according to 0%–30% ITE contents (Fig. 3c). During the forward sweep, the devices that had 0% and 10% ITE did not emit light at $V_{DS} > -3.0$ V, and V_{on} increased from −2.74 V at 20% to −2.02 V at 30%. In MEH-PPV, holes are more mobile than electrons, and electron injection is much slower than hole injection, even with cation EDLs and low-work-function cathodes[31–33]. Therefore, this facilitation of turn-ON behaviour with increasing ITE content is primarily attributed to improved electron injection for radiative recombination in a single-active-layer device. Furthermore, the EOLETs that had 20% and 30% ITE content emitted light even at V_{DS} lower than the energy-gap potential ($|V_{DS}| < |E_g/e| \approx 2.17$ V); this result also confirms that EDL formation at the drain electrode by cation migration overcomes the electron injection barrier[31,34].

The spatial distribution of injected cations was measured using ex situ time-of-flight secondary ion mass spectrometry for pristine and ITE 20% films (Fig. 3d). In the EOLET device, we maintained operation for 30 s under specific conditions ('As fabricated' without voltage application versus 'OFF state' with $V_{DS} = -2.5$ V and $V_{GS} = 0$ V) and then removed the electrolyte layer to fix the migrated cations in the LEP films. For pristine MEH-PPV, the cation ($EMIM^+$) signal intensity within the LEP film remained unchanged across the as-fabricated and OFF states, indicating minimal changes in cation distribution under V_{DS} application. By contrast, the 20% ITE film exhibited a substantial increase in cation signal intensity under V_{DS} application. These results confirm cation migration towards the drain electrode at the OFF state and suggest that a spatial cation distribution through the LEP film on the drain electrode can be maintained.

The absence of n-type doping during p-channel formation and PRZ formation at the drain electrode were verified using the in situ Raman spectroscopy analysis of EOLET with the 20% ITE film (Fig. 3e and Supplementary Fig. 12). The Raman peaks were assigned at vibrational modes of MEH-PPV at 1,623 cm^{-1} (vinyl ν(C=C)), 1,581 cm^{-1} (phenyl ring ν(C=C)), 1,310 cm^{-1} (vinyl ν(C=C) + δ(C=C–H)), 1,283 cm^{-1} (ring ν(C=C) + δ(C=C–H)), and 967 and 1,110 cm^{-1} (β(C=C–H))[35]. Under constant $V_{GS} = 0$ V and $V_{DS} = -2.5$ V, the peak positions did not change from those of the as-fabricated samples without voltage application; this result implies that only EDLs were formed without electrochemical doping that typically causes significant peak shifts in the Raman spectrum[36,37]. The application of constant $V_{GS} = -2.5$ V induced a significant peak shift from 1,581 cm^{-1} (phenyl ring ν(C=C)) to 1,546 cm^{-1} near the source electrode. This substantial peak shift in the vibrational mode at the phenyl ring of the MEH-PPV backbone is evidence of a conformational transition from benzoid to quinoid with polaron formation due to electrochemical p-type doping[36,37]. By contrast, LEP on the drain electrode showed Raman signals with increased background; this change implies that the background overlaps with luminescence signals generated by charge carrier recombination[35]. Additionally, the redshift in the Raman peak of MEH-PPV at the drain electrode was also observed. When electrochemical p-type doping occurs, exciton quenching in LEPs can simultaneously occur; therefore, light emission hardly occur at the electrochemically doped regions[38]. Therefore, this result implies that a p-channel is formed at the top of the channel, and simultaneously, charge carrier recombination occurs near the drain electrode at the bottom of the channel. Consequently, Raman analysis supports the mechanisms of PRZ formation without n-type doping.

The electrical and optical transfer characteristics of EOLETs were also measured by forward and subsequent backward sweeps from $V_{GS} = 0$ V to −2.5 V with constant $V_{DS} = -2.5$ V (Fig. 3f, Supplementary Fig. 13 and Supplementary Table 2). In the electrical transfer curves, maximum I_{DS} changed from ITE 0% to ITE 10% but then greatly increased to ITE 20% and decreased again at ITE 30%. This trend

https://doi.org/10.1038/s41563-026-02613-7

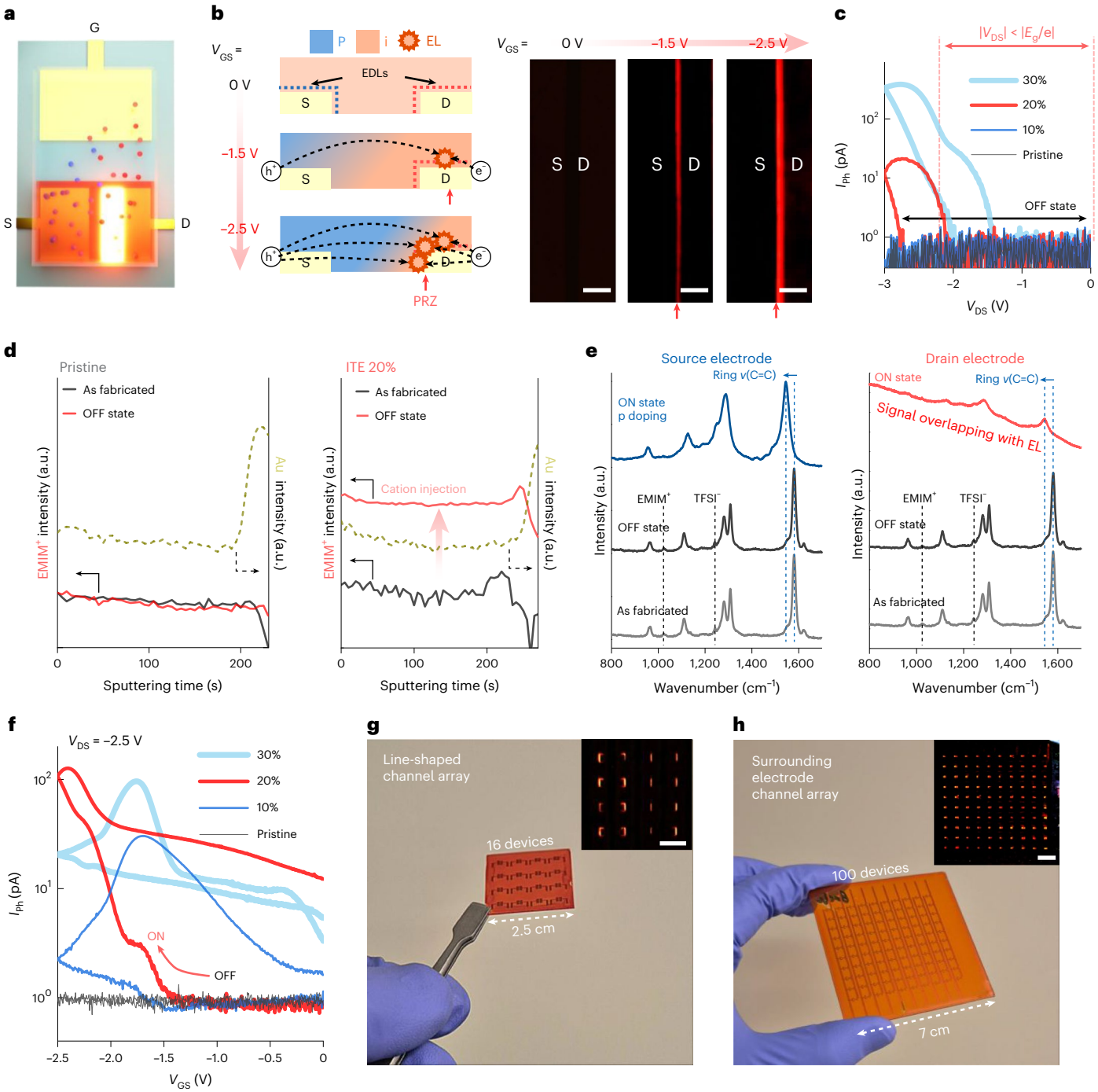

Fig. 3 | Operating mechanisms of EOLETs with drain-side EDL. a, Schematics of EOLET with a lateral gate. **b**, Operating mechanisms and in situ optical microscopic images of EOLET in operation with constant V_{DS} = −2.5 V. Due to stable EDL formation without electrochemical doping, the position of the recombination zone does not change with V_{GS}. Scale bar, 100 µm. **c**, Forward and subsequent backward sweeps from V_{DS} = 0 V to −2.5 V with fixed V_{GS} = −1.0 V according to the ITE content. EOLET devices with 20% or 30% ITE emitted light at $|V_{DS}|$ lower than the energy-gap potential ($|V_{DS}| < |E_g/e|$) of MEH-PPV. **d**, Ex situ time-of-flight secondary ion mass spectrometry doping profile of pristine and ITE 20% films. **e**, In situ Raman spectroscopy measurements of LEP channel on source and drain electrodes for the verification of operating mechanism. During the OFF state, a stable EDL forms without electrochemical doping. During the ON state, electrochemical doping occurs at the source electrode to form p-channels, and radiative recombination occurs at the drain electrode. **f**, Optical transfer curves of EOLET with constant V_{DS} = −2.5 V according to the ITE content. **g**, EL image of a 4 × 4 EOLET array with line-shaped channel electrodes, showing uniform emission and geometric flexibility. Scale bars, 1 cm (inset). **h**, EL image of a 10 × 10 EOLET array with the surrounding electrode channel, confirming large-area integration and high device density. Both array formats highlight the universality of the solution-based fabrication process. Scale bars, 1 cm (inset).

confirmed that a polar polyethylene glycol group of ITE improved ion transport within the channel, and therefore, the maximum I_{DS} increased up to ITE 20% due to improved electrochemical p-type doping efficiency of the LEP. In the optical characteristics, initially, the device with 0% ITE did not emit light, but the devices that had 10%, 20% and 30% ITE emitted light; the maximum I_{Ph} increased as the ITE content increased from 10% to 20%, but the device with 30% showed decreased I_{Ph} with unstable always-ON operation (Fig. 3f). This instability also caused the

lower I_{DS} relative to 20% ITE, owing to excessive ITE that disrupts stable EDL formation without n-type doping. These results show that stable ON/OFF EOLET operation is achieved at 10%–20% ITE.

To further verify the role of cation migration in electron injection, we examined the effects of drain-side cation accumulation and ITE molecular structure (Supplementary Fig. 14 and Extended Data Fig. 2). In the 0% ITE device, positive V_{GS} increased the cation population near the drain electrode and enhanced I_{Ph}, confirming that cation accumulation facilitates electron injection (Supplementary Fig. 14). We also found that increasing the glycol-chain length of the ITE increased I_{Ph} and lowered V_{th}, consistent with the effect of increasing ITE content (Extended Data Fig. 2). These results show that stable EOLET operation with a PRZ requires controlled cation migration to form a drain-side cation EDL without electrochemical n-type doping.

To demonstrate the scalability and geometric adaptability of our approach, we fabricated two types of EOLET array using solution-processed LEP films containing 20% ITE. A 4 × 4 array with line-shaped channels was fabricated on a 2.5 × 2.5-cm^2 area (Fig. 3g), resulting in a resolution of approximately 2.88 pixels per inch (ppi). Additionally, a 10 × 10 array using surrounding electrode channels was fabricated on a 7 × 7-cm^2 substrate (Fig. 3h and Supplementary Fig. 15), corresponding to a resolution of 2.56 ppi. This array demonstrated the simultaneous operation of 100 pixels with stable and uniform EL. These array demonstrations show that each device maintained spatially pinned emission during operation, confirming robust PRZ formation and highlighting the geometric versatility, large-area scalability and array-level uniformity of the material system for practical display applications.

Flexible and large-area EOLETs

We next fabricated flexible and large-area EOLETs for practical wearable display applications (Fig. 4a). The large-area EOLET was composed of a polyethylene terephthalate substrate, a silver nanowire (AgNW) lateral gate electrode, 20% ITE-LEP and Au source/drain electrodes. The EOLET, designed with centimetre-scale interdigitated channel electrodes, achieves stronger light emission and a wider RZW compared with the small EOLET, making it well suited for practical display applications. This enhancement is attributed to the higher $|V_{DS}| = 3.5$ V in the large EOLET compared with $|V_{DS}| = 2.5$ V for the small EOLET. To maintain a stable OFF state despite the increased $|V_{DS}|$, we designed the channel length to be 500 µm, effectively preventing unintended light emission in the OFF state and ensuring reliable device operation (Extended data Fig. 3a).

To clarify the EOLET geometry and operating mechanism, we analysed the lateral AgNW gate structure and gate coupling behaviour (Extended Data Fig. 3). Electrochemical impedance spectroscopy showed a gate capacitance of 5.2 µF cm^{-2} for the poly(vinylidene fluoride-*co*-hexafluoropropylene) (PVDF-HFP) electrolyte, which arises predominantly from EDLs formed at the electrode/electrolyte interfaces rather than from bulk polarization, consistent with the Poisson–Boltzmann prediction that the potential drops within a few nanometres of the interface and the electric field in the bulk electrolyte becomes negligible owing to efficient ionic screening (Extended Data Fig. 3b)[39,40]. Consistent with this interfacial gating mechanism, the AgNW electrode exhibited a much larger interfacial capacitance than the LEP channel, allowing most of the gate voltage to be effectively dropped across the channel and, therefore, enabling efficient electrochemical modulation (Extended Data Fig. 3c). In addition, ITE incorporation increased the channel capacitance and volumetric capacitance C^* of the LEP, indicating enhanced ion penetration and doping, which further strengthened electrochemical gating efficiency. Thus, the EOLET can efficiently modulate the channel using AgNW gate electrodes, and the incorporation of ITE further enhances this modulation by increasing C^*, thereby improving the OLET performance under reduced V_{GS}.

We next evaluated the electrical and optical transfer characteristics of large-area EOLETs to validate the transistor operation and light emission controllability (Supplementary Fig. 16). The electrical transfer curves revealed an ON/OFF ratio exceeding 10^4, and negligible gate leakage I_{GS} in the ON state, which remained approximately three orders of magnitude lower than I_{DS} at $V_{GS} = -3.5$ V, validating stable and efficient operation. The maximum luminance of the large-area EOLET reached 536 cd m^{-2} with a stable emission profile. The turn-ON V_{GS}, defined as the V_{GS} at which luminance exceeds 1 cd m^{-2} (ref. 41), was observed at −2.0 V. Additionally, the devices showed a large hysteresis window of ~0.65 V in the transfer curve, suggesting ion-induced memory characteristics. The electrical output characteristics further support the robust transistor operation of EOLET with PRZ (Supplementary Fig. 17). Furthermore, EOLET with ITE 20% achieved a maximum external quantum efficiency of 0.50% during transfer curve measurements, whereas the device without ITE exhibited no optical turn-ON (Supplementary Fig. 18). These results highlight the robustness of the PRZ mechanism in ensuring gate-controllable light emission and demonstrate the feasibility of using this platform for low-voltage OLET applications.

To further understand the formation and tunability of the recombination zone in the PRZ-based EOLET, we analysed the dependence of RZW on both V_{GS} and V_{DS} (Fig. 4c and Supplementary Fig. 19). In lateral-channel EOLETs, charge transport proceeds horizontally, and holes and electrons meet for radiative recombination at specific regions within the channel; therefore, increasing the RZW is the main challenge for practical applications of EOLETs[42]. The greyscale-processed images were used to extract RZW under two different biasing conditions (Supplementary Fig. 19). When sweeping V_{DS} from −1.5 V to −3.5 V at a fixed gate voltage ($V_{GS} = -1.5$ V), the RZW broadened from 0 µm to 267 µm, indicating enhanced electron injection due to increased voltage between the LEP channel and Au electrodes. In particular, the observable light emission was detected at $V_{DS} = -2.0$ V, which is below the bandgap potential ($|V_{DS}| < E_g/e \approx 2.17$ V), confirming that the cationic EDL at the drain electrode effectively facilitates electron injection even at sub-bandgap voltages. In a separate V_{GS} sweep with fixed $V_{DS} = -3.5$ V, the RZW also broadened with increasing $|V_{GS}|$, reaching a maximum of 264 µm at −3.5 V. This trend suggests enhanced hole transport from the source electrode under stronger gate-induced p-type doping. Interestingly, whereas both biasing conditions resulted in a broad PRZ formation, the RZW under the V_{GS} sweep begins at approximately 176 µm, whereas the RZW under the V_{DS} sweep starts near 0 µm. This difference arises because V_{DS} is fixed at −3.5 V during the V_{GS} sweep, ensuring sufficient electron injection from the drain electrode throughout the measurement. These results confirm that both electron and hole injection processes play essential roles in PRZ formation and demonstrate that our material system enables spatially extended and voltage-tunable recombination zones by effectively controlling the charge injection and transport mechanisms in OLETs. This drain-side EDL-based charge injection mechanism enabled an unprecedentedly wide RZW compared with both field-effect and electrochemical p–i–n junction mechanisms, which typically show dynamic recombination zones and for which the absolute luminance values have rarely been reported (Fig. 4d and Supplementary Table 3). Thus, our strategy represents a significant advance towards practical single-active-layer EOLETs that combine ultralow-voltage operation and multifunctionality in a simple device structure.

We further evaluated the environmental and operational stabilities of the EOLET platform. The current–voltage characteristics of Au/AgNW/Au and Au/AgNW/electrolyte/Au structures remained essentially unchanged after 21 days in ambient air, confirming the stability of both AgNW network and electrode–electrolyte interface (Supplementary Fig. 20). Under continuous bias stress, the EOLET maintained a stable current flow and EL for over 23,000 s, with an L_{70} value of 13,300 s from an initial luminance of 230 cd m^{-2},

https://doi.org/10.1038/s41563-026-02613-7

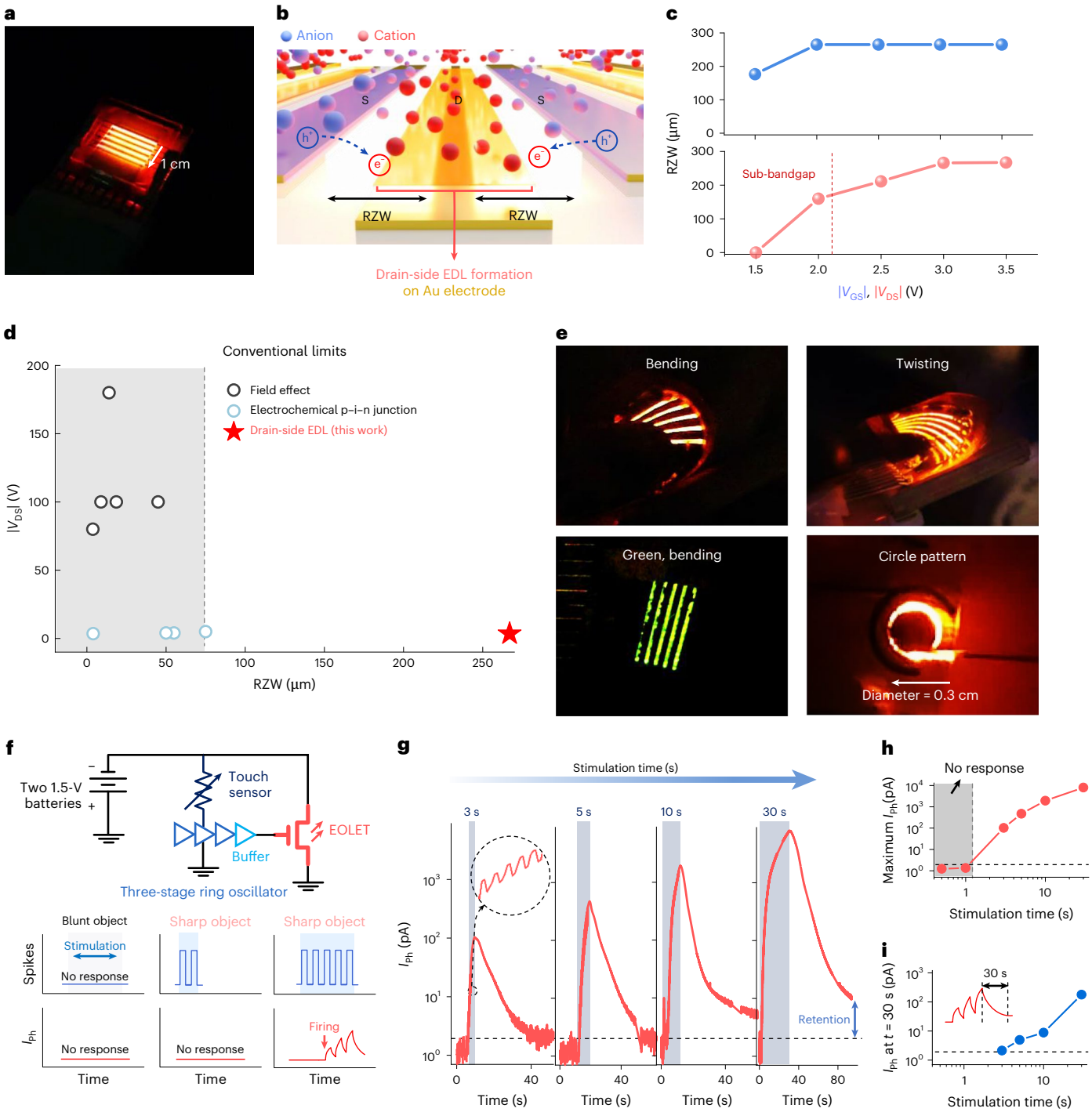

Fig. 4 | Flexible and large-area EOLETs. a, Photographs of large-area EOLET in ON states ($V_{GS} = V_{DS} = -3.5$ V). **b**, Schematics of the operating mechanism of large-area EOLET. **c**, RZW depending on V_{DS} and V_{GS}, indicating the enhancement of electron injection and hole transport, respectively. **d**, Comparison of EOLET performance with reported single-active-layer OLETs. **e**, Photographs of flexible EOLET being bent and twisted, and of different patterns and colours. **f**, Schematic of the SAND system: flexible touch sensor, flexible ring oscillator, flexible EOLET and two 1.5-V batteries. This system has an intrinsic threshold for response to weak stimuli (for example, touch by a blunt object, brief touch by a sharp object), as do biological nerves. **g**, Visual spike responses of SAND versus simulation duration. Stimuli are encoded to spike signals and induce visual responses due to the synaptic plasticity of EOLET. **h**, Maximum I_{Ph} of SAND versus stimulation duration. **i**, Retentive I_{Ph} at 30 s after stimulation. In **g**–**i**, the grey dashed lines represent the noise levels.

demonstrating substantially improved operational stability compared with conventional p–i–n OLETs (Supplementary Fig. 21 and Supplementary Table 3)[19].

We next evaluated the flexibility and mechanical stability of EOLETs fabricated on a flexible substrate (Fig. 4e and Supplementary Video 1). Due to the centimetre-scale interdigitated electrodes, p-channels and recombination zones were formed on both sides of the drain electrodes, enabling bright and wide emissions suitable for practical applications. Moreover, due to the flexible nature of the LEP and electrolytes, the EOLET emitted stably and brightly under repetitive bending and twisting motions (Supplementary Video 1). A flexible and large-area EOLET was also achieved using various emission patterns, such as linear and circular.

Furthermore, the ITE incorporation strategy was extended to green fluorescent and thermally activated delayed fluorescence LEPs, confirming the broad applicability of our material design (Extended Data Fig. 5 and Supplementary Fig. 22). A comparative analysis of LEPs showed that ITE blending consistently improved I_{DS} and I_{Ph} across all LEPs, whereas the best EOLET performance was obtained with MEH-PPV/ITE, which exhibited the highest C^* and enabled the lowest operating voltage and strongest I_{Ph} despite its lower PL quantum yield. These results may indicate LEPs with high electrochemical gating capability as the most suitable materials for our EOLET platform.

The luminescence performance of the EOLET was further improved by introducing the ionic additive TBA-BF_4 into the LEP channel, and maintaining the PRZ (Extended Data Fig. 6). The presence of uncompensated ionic charges near the channel electrode interface may facilitate charge injection, resulting in enhanced radiative recombination within the single-active-layer. Consequently, the device with a TBA-BF_4 content of 20 wt% exhibits a maximum luminance of 826 cd m^{-2} and an EQE of 1.04%, together with a spatially pinned emission profile extending over approximately 247 µm. These results indicate that the precise control of ion transport in the LEP channel, rather than indiscriminate enhancement, is essential for stable OLET operation.

We further applied the EOLET to a stand-alone neuromorphic display (SAND) that mimics biological pain perception, motivated by the need for intelligent portable systems that can protect patients with pain-insensitivity disorders from harmful stimuli[43]. To meet this goal, the platform must support low-voltage battery operation, large-area light emission and mechanical flexibility for on-skin use. As a proof of concept, we integrated a flexible touch sensor, a flexible ring oscillator, a flexible EOLET and two 1.5-V batteries into a stand-alone flexible system (Fig. 4f and Supplementary Fig. 23). The device generated spike signals only in response to potentially harmful stimuli, whereas innocuous inputs were filtered out by the threshold response of the EOLET (Extended Data Fig. 7). Under sustained strong stimulation, both maximum and retained I_{Ph} gradually increased after 30 s, indicating synaptic plasticity on timescales relevant to human touch and interaction (Fig. 4g–i). These results demonstrate low-voltage intelligent sensory processing with visual outputs in a wearable format.

Outlook

In summary, we demonstrate a single-active-layer EOLET that achieves ultralow-voltage operation (<3.5 V) and an exceptionally wide recombination zone (~267 µm), addressing the fundamental limitations of OLETs. By incorporating an ITE into the LEP channel, efficient ionic transport is enabled without introducing additional charge injection or transport layers, leading to the formation of EDLs at the drain electrode interface that overcome the intrinsic electron injection barrier and allow light emission at drain voltages even below the bandgap potential of the polymer channel. Unlike conventional EOLETs relying on dynamic p–i–n junction formation, this work prevents the formation of n-type doping fronts and exhibits a spatially PRZ that remains stable irrespective of the gate voltage. As a result, the device achieves an unprecedented RZW of up to 267 µm and a maximum luminance of 826 cd m^{-2} at V_{DS} = −3.5 V, preserving a simple single-active-layer architecture and mechanical flexibility. This work establishes a new operating regime for OLETs, providing a mechanistic insight into achieving low-voltage and spatially pinned light emission in simple organic transistor architectures and laying the foundation for future user-interactive organic electronic systems with intuitive visual feedback.

Online content

Any methods, additional references, Nature Portfolio reporting summaries, source data, extended data, supplementary information, acknowledgements, peer review information; details of author contributions and competing interests; and statements of data and code availability are available at https://doi.org/10.1038/s41563-026-02613-7.

References

1. Jiang, Y. et al. A universal interface for plug-and-play assembly of stretchable devices. *Nature* **614**, 456–462 (2023).
2. Li, P. et al. N-type semiconducting hydrogel. *Science* **384**, 557–563 (2024).
3. Hong, S. J. et al. Bio-inspired artificial mechanoreceptors with built-in synaptic functions for intelligent tactile skin. *Nat. Mater.* **24**, 1100–1108 (2025).
4. Tan, Y. J. et al. A transparent, self-healing and high-κ dielectric for low-field-emission stretchable optoelectronics. *Nat. Mater.* **19**, 182–188 (2020).
5. Li, N. et al. Immune-compatible designs of semiconducting polymers for bioelectronics with suppressed foreign-body response. *Nat. Mater.* **25**, 124–132 (2026).
6. Zhao, C. et al. Skin-like drift-free biosensors with stretchable diode-connected organic field-effect transistors. *Nat. Electron.* **8**, 981–993 (2025).
7. Jung, H. et al. Hydrogel–elastomer-based conductive nanomembranes for soft bioelectronics. *Nat. Nanotechnol.* **20**, 1822–1830 (2025).
8. Nishio, Y. et al. Intrinsically stretchable transistors and integrated circuits. *Nat. Rev. Electr. Eng.* **2**, 715–735 (2025).
9. Wang, T. et al. A chemically mediated artificial neuron. *Nat. Electron.* **5**, 586–595 (2022).
10. Wang, W. et al. Neuromorphic sensorimotor loop embodied by monolithically integrated, low-voltage, soft e-skin. *Science* **380**, 735–742 (2023).
11. Kim, Y. et al. A bioinspired flexible organic artificial afferent nerve. *Science* **360**, 998–1003 (2018).
12. Sung, M.-J. et al. Organic artificial nerves: neuromorphic robotics and bioelectronics. *Chem. Rev.* **125**, 2625–2664 (2025).
13. Hepp, A. et al. Light-emitting field-effect transistor based on a tetracene thin film. *Phys. Rev. Lett.* **91**, 157406 (2003).
14. Capelli, R. et al. Organic light-emitting transistors with an efficiency that outperforms the equivalent light-emitting diodes. *Nature Mater.* **9**, 496–503 (2010).
15. Zaumseil, J., Donley, C. L., Kim, J.-S., Friend, R. H. & Sirringhaus, H. Efficient top-gate, ambipolar, light-emitting field-effect transistors based on a green-light-emitting polyfluorene. *Adv. Mater.* **18**, 2708–2712 (2006).
16. Hou, L. et al. Optically switchable organic light-emitting transistors. *Nat. Nanotechnol.* **14**, 347–353 (2019).
17. Liu, J., Engquist, I., Crispin, X. & Berggren, M. Spatial control of p–n junction in an organic light-emitting electrochemical transistor. *J. Am. Chem. Soc.* **134**, 901–904 (2012).
18. Liu, J., Engquist, I. & Berggren, M. Double-gate light-emitting electrochemical transistor: confining the organic p–n junction. *J. Am. Chem. Soc.* **135**, 12224–12227 (2013).
19. Liu, J., Engquist, I. & Berggren, M. Half-gate light-emitting electrochemical transistor to achieve centered emissive organic p–n junction. *Org. Electron.* **18**, 32–36 (2015).
20. Bhat, S. N., Pietro, R. D. & Sirringhaus, H. Electroluminescence in ion-gel gated conjugated polymer field-effect transistors. *Chem. Mater.* **24**, 4060–4067 (2012).
21. Kim, J.-H. & Park, J.-W. Intrinsically stretchable organic light-emitting diodes. *Sci. Adv.* **7**, eabd9715 (2021).
22. Zhang, Z. et al. High-brightness all-polymer stretchable LED with charge-trapping dilution. *Nature* **603**, 624–630 (2022).
23. Cossiello, R. F. et al. Photoluminescence and relaxation processes in MEH–PPV. *Macromolecules* **38**, 925–932 (2005).
24. Wang, R. et al. Effect of thermal annealing on aggregations in MEH–PPV films. *J. Phys. Chem. C* **123**, 11055–11062 (2019).
25. Koo, J. et al. Low-power, deformable, dynamic multicolor electrochromic skin. *Nano Energy* **78**, 105199 (2020).

26. Guo, J. et al. Understanding asymmetric switching times in accumulation mode organic electrochemical transistors. *Nat. Mater.* **23**, 656–663 (2024).
27. Keene, S. T. et al. A biohybrid synapse with neurotransmitter-mediated plasticity. *Nat. Mater.* **19**, 969–973 (2020).
28. Sung, M. et al. Overcoming the trade-off between efficient electrochemical doping and high state retention in electrolyte-gated organic synaptic transistors. *Adv. Funct. Mater.* **34**, 2312546 (2024).
29. Ohayon, D., Druet, V. & Inal, S. A guide for the characterization of organic electrochemical transistors and channel materials. *Chem. Soc. Rev.* **52**, 1001–1023 (2023).
30. Paterson, A. F. et al. On the role of contact resistance and electrode modification in organic electrochemical transistors. *Adv. Mater.* **31**, 1902291 (2019).
31. Yasuji, K., Sakanoue, T., Yonekawa, F. & Kanemoto, K. Visualizing electroluminescence process in light-emitting electrochemical cells. *Nat. Commun.* **14**, 992 (2023).
32. Amorim, C. A. et al. Determination of carrier mobility in MEH-PPV thin-films by stationary and transient current techniques. *J. Non-Cryst. Solids* **358**, 484–491 (2012).
33. Zhou, H. et al. Graphene-based intrinsically stretchable 2D-contact electrodes for highly efficient organic light-emitting diodes. *Adv. Mater.* **34**, 2203040 (2022).
34. Slinker, J. D. et al. Direct measurement of the electric-field distribution in a light-emitting electrochemical cell. *Nat. Mater.* **6**, 894–899 (2007).
35. Moraes, B. R., Campos, N. S., Barra, A. C. C. & Izumi, C. M. S. Surface-enhanced Raman scattering of MEH-PPV on gold and silver nanoparticles. *J. Spectrosc.* **2018**, 6924758 (2018).
36. Dong, W. S. et al. Frequency-dependent learning achieved using semiconducting polymer/electrolyte composite cells. *Nanoscale* **7**, 16880–16889 (2015).
37. Baïtoul, M. et al. Evidence of electron-hole symmetry breaking in poly(*p*-phenylene vinylene). *Phys. Rev. B* **68**, 195203 (2003).
38. Van Reenen, S., Vitorino, M. V., Meskers, S. C. J., Janssen, R. A. J. & Kemerink, M. Photoluminescence quenching in films of conjugated polymers by electrochemical doping. *Phys. Rev. B* **89**, 205206 (2014).
39. Melzer, K. et al. Characterization and simulation of electrolyte-gated organic field-effect transistors. *Faraday Discuss.* **174**, 399–411 (2014).
40. Tu, D. et al. A static model for electrolyte-gated organic field-effect transistors. *IEEE Trans. Electron Devices* **58**, 3574–3582 (2011).
41. Han, S. J., Zhou, H., Kwon, H., Woo, S. & Lee, T. Achieving low-voltage operation of intrinsically-stretchable organic light-emitting diodes. *Adv. Funct. Mater.* **33**, 2211150 (2023).
42. Ganesan, P., Tsao, H. N. & Gao, P. En route to wide area emitting organic light-emitting transistors for intrinsic drive-integrated display applications: a comprehensive review. *Adv. Funct. Mater.* **31**, 2105506 (2021).
43. Lischka, A. et al. Genetic pain loss disorders. *Nat. Rev. Dis. Primers* **8**, 41 (2022).

Methods

Preparation of LEP and electrolyte solutions

For pristine solutions (ITE = 0%), MEH-PPV (average M_n 40,000–70,000, Sigma-Aldrich) was dissolved in cyclohexanone (Sigma-Aldrich) at a concentration of 10 mg ml^{-1}. For blend solutions, ITE (Triton X-100, Sigma-Aldrich) was first dissolved at 10 mg ml^{-1} in cyclohexanone. MEH-PPV and ITE solutions were mixed according to the blend ratio ratios (ITE content = $100 \times w_{Surfactant}/w_{LEP}$, where w is the weight). Additional cyclohexanone was added to each ITE solution at 12 mg ml^{-1} of MEH-PPV. The LEP solutions were stirred using a magnetic stirrer at 50 °C overnight. ITE with n = 12 (IGEPAL CA-720, Sigma-Aldrich) and n = ~5 (Triton X-45, Sigma-Aldrich), and poly[(9,9-dioctyl-2,7-divinylene-fluorenylene)-*alt*-*co*-(2-methoxy-5-(2-ethylhexyloxy)-1,4-phenyene)] solutions were prepared using the same method.

Poly(vinylidene fluoride-*co*-hexafluoropropylene) (Sigma-Aldrich), 1-ethyl-3-methylimidazolium bis(trifluoromethylsulfonyl) imide (Sigma-Aldrich) and acetone (Sigma-Aldrich) were mixed at a weight ratio of 1:4:10 and stirred using a magnetic stirrer at 50 °C overnight to prepare an electrolyte solution.

Fabrication of EOLET for mechanistic characterization

First, both channel and gate electrodes were fabricated by the thermal evaporation of Au (30 nm)/Cr (5 nm) on glass. The LEP solutions were spin coated on the channel electrodes at 2,000 rpm for 60 s and then annealed at 90 °C for 20 min. On the LEP/channel electrodes, the electrolyte film was fabricated by the drop casting of the electrolyte solution, dried in ambient conditions overnight and then transferred by a cut-and-paste method.

Fabrication of large and flexible EOLET

First, a AgNW-embedded electrolyte film was fabricated as follows. A dispersion (5 mg ml^{-1} in isopropyl alcohol, Novarials) of AgNWs (30 nm × 30 μm), was spin coated on the glass substrate and then annealed at 100 °C for 5 min. Then, the electrolyte solution was drop cast on the AgNW layer and then dried in ambient conditions overnight to form an AgNW-embedded electrolyte film. AgNW-embedded electrolyte film was peeled from the glass substrate and transferred by a cut-and-paste method onto the LEP/channel electrodes on a flexible polyethylene terephthalate substrate.

Characterization of LEP films

LEP films were fabricated on glass and ITO electrodes on a glass substrate for the subsequent analysis. GIXD images were collected at beamline 11-3 of the Stanford Synchrotron Radiation Lightsource using a two-dimensional area detector in a helium chamber to minimize air-scattering background. The sample-to-detector distance was set to 300 mm and the incidence angle was 0.12°. The X-ray wavelength was 0.9758 Å (12.735 keV). The PL was measured using spectrofluorometry (JASCO FP8500). The surface topology and phase were measured using atomic force microscopy (NX-10, Park Systems). The absorbance was measured using UV absorption spectroscopy (Lambda 465, PerkinElmer). The Raman signals were measured using a Raman spectrometer (LabRAM HR Evolution, HORIBA). For in situ UV–vis spectroscopy and Raman spectroscopy measurements, a semiconductor analyser (Keithley 2602 system source meter, Keysight) was used.

Characterization of EOLET

Electrical measurements were conducted using a semiconductor device analyser (Keithley B1500A, Keysight), and I_{Ph} was directly recorded by a photodiode (818 UV/DB Optical Power Detector, Newport) without additional normalization or post-processing, enabling the millisecond-scale resolution of transient optical responses. The luminance and external quantum efficiency of the device were measured using an integrating sphere (Labsphere) coupled to a PMA-12 charge-coupled device spectrometer (Hamamatsu) to collect the emitted light.

Fabrication and characterization of wearable SAND

The flexible touch sensor was fabricated using polydimethylsiloxane (PDMS) (SYLGARD184, Dow Corning) and Au electrodes. First, Au (30 nm) was thermally deposited on PDMS (precursor:crosslinker = 10:1 weight ratio) film, and two Au/ PDMS were stacked with a PDMS spacer. The ring oscillator was composed of complementary metal–oxide–semiconductor inverters (CD4007UBM, HGSEMI) and capacitors (CL31A106KBHNNNE, Samsung Electro-Mechanics). The electrical measurement of the ring oscillator was performed using an oscilloscope (54832D Mixed Signal Infiniium Oscilloscope, Keysight)

The SAND was constructed by connecting the flexible touch sensor, flexible ring oscillator, flexible EOLET with 20% ITE-LEP and two 1.5-V batteries (AA alkaline battery, ZHONGTIN (NINGBO) BATTERY). The photocurrent of SANDs was measured using a photodiode (818 UV/DB Optical Power Detector, Newport) and Keithley B1500A. For on-skin applications, SAND was attached to an artificial hand by using a transparent skin patch (Tegaderm, 3M)

Data availability

All the data supporting this study are available in the Article and its Supplementary Information. Source data are provided with this paper.

Acknowledgements

K.-N.K. and H.Z. equally contributed to this work. This research was supported by the Pioneer Research Center Program through the National Research Foundation (NRF) of Korea funded by the Ministry of Science and ICT (MSIT) (RS-2022-NR067540). This work was also supported by the NRF grant funded by the Ministry of Science and ICT (MSIT) (RS202500560490). K.-N.K. and T.-W.L. were supported by the Korea Institute of Energy Technology Evaluation and Planning (KETEP) grant funded by the Korean Ministry of Trade, Industry and Energy (MOTIE) (20214000000570).

Author contributions

K.-N.K., H.Z. and T.-W.L. conceived the research idea. K.-N.K. and H.Z. fabricated the EOLET devices and analysed data. K.-N.K., H.Z. M.-J. S. and D.-G.S. designed the EOLET devices with the gold gate electrode. K.-N.K., H.Z., W.J.J. and Jinwoo Park conducted the measurement and analysis of photocurrent, luminance and efficiency of EOLETs. Y.W. and Z.B. conducted the GIXD measurement and analysis. K.-N.K. and D.-Y.K. conducted the in situ UV–vis spectroscopy measurement. K.-N.K. and H.Z. conducted the in situ optical microscopy and ex situ time-of-flight secondary ion mass spectroscopy measurements. S.L. and H.-L.P. fabricated the flexible PCB. K.-N.K., H.Z. and Z.B. designed the flexible and large-area EOLET. K.-N.K., H.Z., Y.L., K.K.K., Jaeho Park and Z.B. designed the SAND systems and performed the wearable applications. Y.C. synthesized the thermally activated delayed fluorescence LEP. K.-N.K. drafted the first version of the manuscript, with assistance from H.Z. and T.-W.L. All authors contributed to the final manuscript. T.-W.L. supervised the research project.

Competing interests

The authors declare no competing interests.

Additional information

Extended data is available for this paper at https://doi.org/10.1038/s41563-026-02613-7.

Supplementary information The online version contains supplementary material available at https://doi.org/10.1038/s41563-026-02613-7.

Correspondence and requests for materials should be addressed to Tae-Woo Lee.

Peer review information *Nature Materials* thanks Ebinazar Namdas, Tatsuo Hasegawa and the other, anonymous, reviewer(s) for their contribution to the peer review of this work.

https://doi.org/10.1038/s41563-026-02613-7

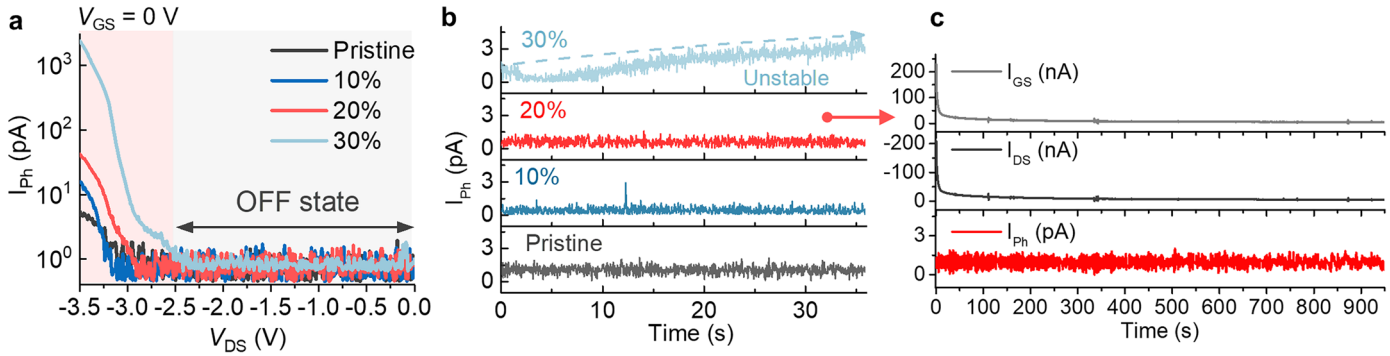

Extended Data Fig. 1 | Determination of OFF state. At the OFF state, the EOLET with 20% ITE did not emit light at $|V_{DS}| < 2.5$ V, and also maintained a clear OFF state without electrochemical doping. (**a**) The OFF-state I_{Ph} was measured starting from V_{DS} = 0 V to −3.5 V with zero gate bias V_{GS} = 0 V. As the ITE content was increased, the OFF-state optical V_{on} of EOLET gradually decreased from −3.18 V at 0% to −3.19 V at 10% to −2.93 V at 20% to −2.49 V at 30%. Simultaneously, the maximum I_{Ph} of EOLET at V_{DS} = − 3.5 V gradually increased from I_{Ph} = 5 pA at 0% to I_{Ph} = 13 pA at 10%, then rapidly from I_{Ph} = 38 pA at 20%, to I_{Ph} = 2225 pA at 30%. This turn-on behavior above V_{on} depending on the V_{DS} may follow the mechanism of EDL formation and subsequent expansion of the doping region in a two-terminal structure. Moreover, the increase in maximum I_{Ph} as ITE content increases, also indicates the ITE facilitates EDL formation and electrochemical doping. With these results, we defined V_{DS} = − 2.5 V as the maximum operation voltage to accomplish both stable operation and sufficient charge injection. For the biasing operation, we also defined V_{GS} = − 2.5 V as the maximum gate bias, because gate bias greater than the channel voltage may induce severe electrochemical doping in the drain electrode by transistor operation, with consequent quenching of electroluminescence. (**b**) The EOLET with 30% ITE showed unstable increase of I_{Ph} at the V_{DS} = − 2.5 V OFF state, so a clear OFF state was not easily defined; therefore, this device does not apply to EOLET operation. Therefore, 20% is the maximum ITE content for high luminance and stable operation of the EOLET. (**c**) The EOLET with 20% ITE showed a stable baseline for 950 s.

https://doi.org/10.1038/s41563-026-02613-7

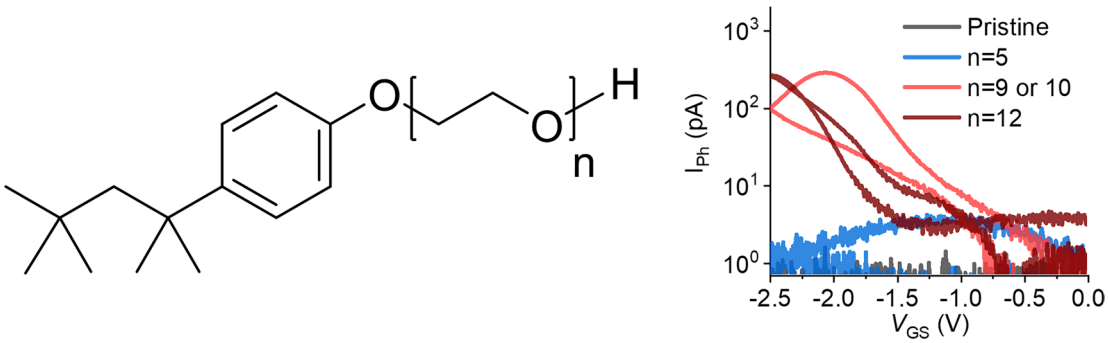

Extended Data Fig. 2 | Optical transfer curves of EOLET according to polar contents in ITE molecules with fixed VDS = − 2.5 V. The molar ratio of ITE molecules to MEH-PPV was 20:1 and we measured the same voltage range as in the optical transfer curves in Fig. 3f. Compared to pristine MEH-PPV, the maximum I_{ph} in the forward sweep increased as glycol content increased from $n = 5$, to n = 9 or 10, but the decrease of I_{ph} during the backward sweep was unstable at $n = 12$. This tendency is the same as the effect of ITE contents (Fig. 3f), so $n = 9$ or 10 is best for stable operation of EOLET. Consequently, this result suggests that the improved luminescent outputs originate from improved ion transport that is a result of the polar group of ITE molecules.

https://doi.org/10.1038/s41563-026-02613-7

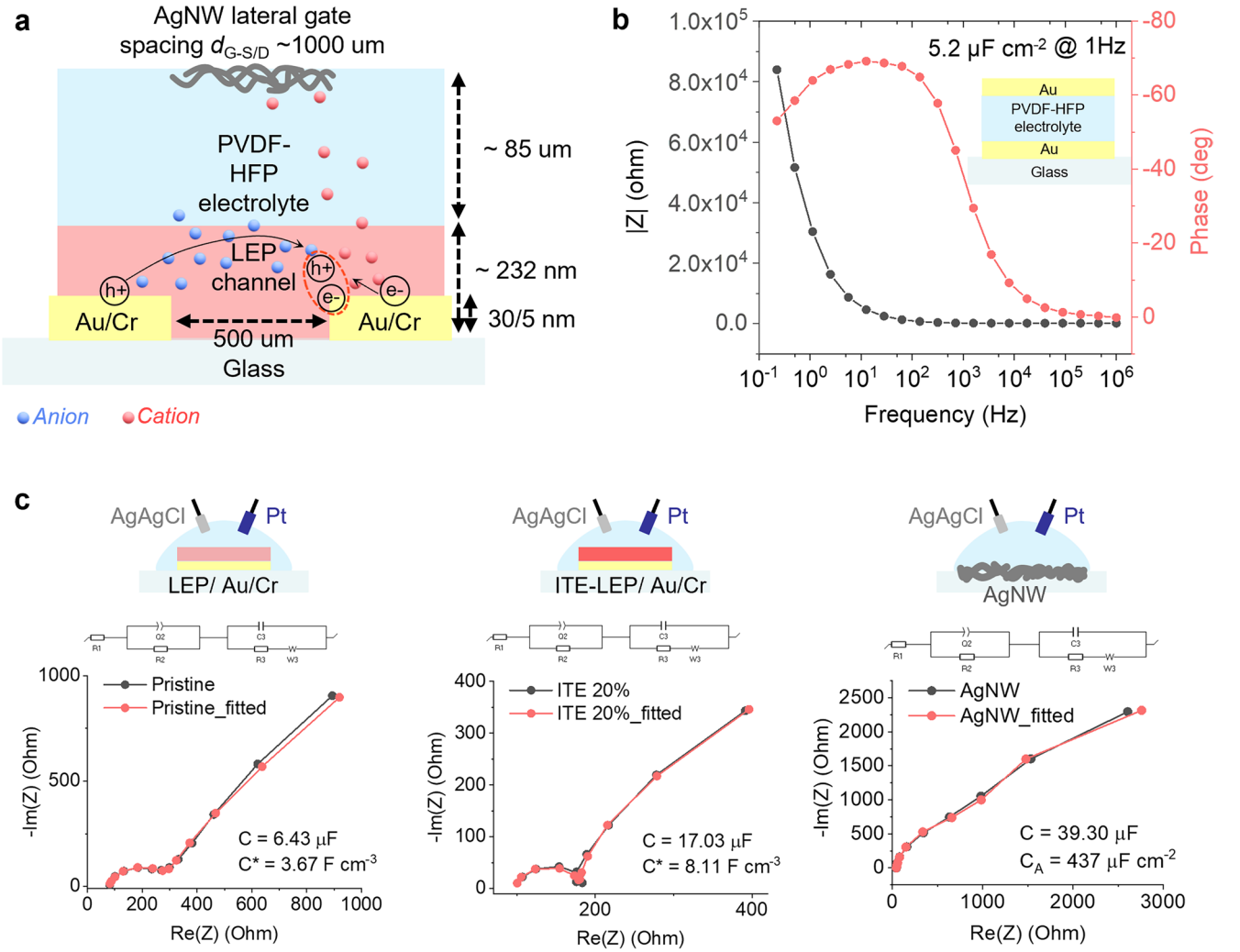

Extended Data Fig. 3 | Gate capacitance analysis of EOLETs. (**a**) Cross-sectional schematic of the EOLET showing the layer thicknesses: ~85 µm PVDF-HFP electrolyte, ~232 nm LEP/ITE active layer, and lateral AgNW gate positioned ~1 mm away from the channel. (**b**) Bode plot of the Au/PVDF-HFP/Au revealing gate capacitance of PVDF-HFP solid electrolyte at 1 Hz. In electrolyte-gated transistors, the gate capacitance is predominantly determined by interfacial electric double layers (EDLs) rather than the bulk properties of the electrolyte. Although the PVDF-HFP dielectric shows a high areal capacitance of 5.2 µF cm^{-2} at 1 Hz, this value arises mainly from interfacial EDL formation, not bulk polarization. The Poisson–Boltzmann equation predicts that electric potential drops occur within a few nanometers of the interface, beyond which the electric field in the bulk electrolyte becomes negligible due to efficient ionic screening[39,40]. As a result, the bulk capacitance contributes insignificantly to the overall gate capacitance and can be omitted from device modeling. These interfacial EDLs using electrolyte enable effective channel modulation at low operating voltages. (**c**) Nyquist plots and equivalent circuit fits for pristine LEP, ITE-LEP, and AgNW configurations. In the electrochemical transistor configuration, the gate capacitance is governed by the series combination of the AgNW/electrolyte interfacial EDL capacitance (C_{AgNW}) and the C_{LEP} and C^* of channel LEPs. C_{AgNW} (39.3 µF) is significantly larger than C_{LEP} (6.43 µF for pristine and 17.03 µF for ITE-LEP) when measured in the same device geometry as the EOLET. This implies that most of the gate voltage can be effectively applied across the LEP channel, ensuring efficient electrochemical modulation even at low bias. Upon blending the ITE, C_{LEP} increases to 17.03 µF from 6.43 µF due to enhanced ion penetration and doping, resulting in a higher C^* = 8.11 F cm^{-3} compared to 3.67 F cm^{-3} for pristine LEP. This also led to an increase in induced hole carrier density to 1.77x10^{20} cm^{-3} from 8.03x10^{19} cm^{-3} for pristine LEP.

https://doi.org/10.1038/s41563-026-02613-7

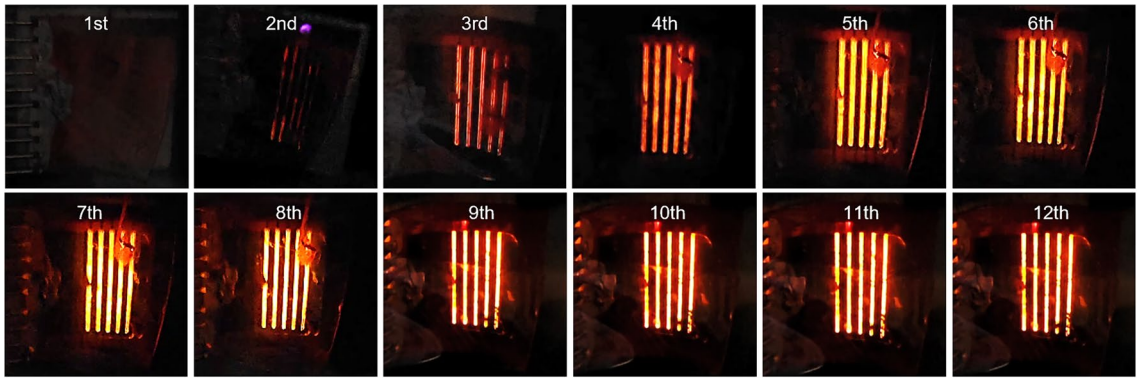

Extended Data Fig. 4 | Spike responses of EOLET with visual outputs during bending. The images were measured at a constant V_{DS} = − 3.5 V with a spike gate voltage V_{GS} = − 3.5 V), applying 5 Hz spike stimulation for 12 cycles, each consisting of 450 spikes, with a 10-second interval between successive cycles.

https://doi.org/10.1038/s41563-026-02613-7

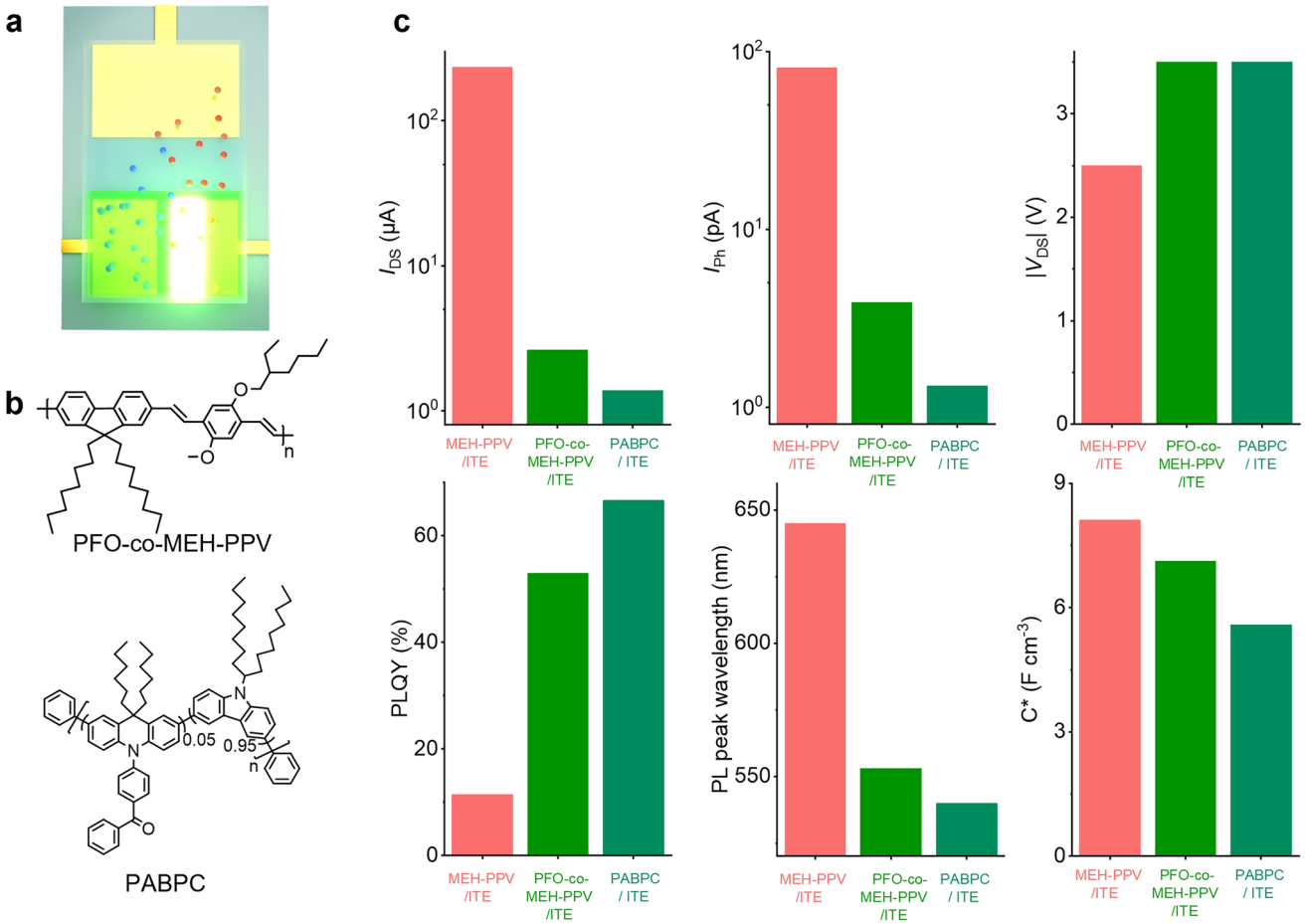

Extended Data Fig. 5 | Universal applicability of EOLETs demonstrated using different LEPs. (**a**) Schematic of an EOLET structure operating as a green-emitting EOLET. (**b**) Molecular structures of PFO-co-MEH-PPV and TADF-type PABPC. (**c**) Comparative electrical, optical, and electrochemical performance metrics across three LEP/ITE systems, including I_{DS}, I_{Ph}, V_{DS}, PLQY, PL peak wavelength, and C^*.

https://doi.org/10.1038/s41563-026-02613-7

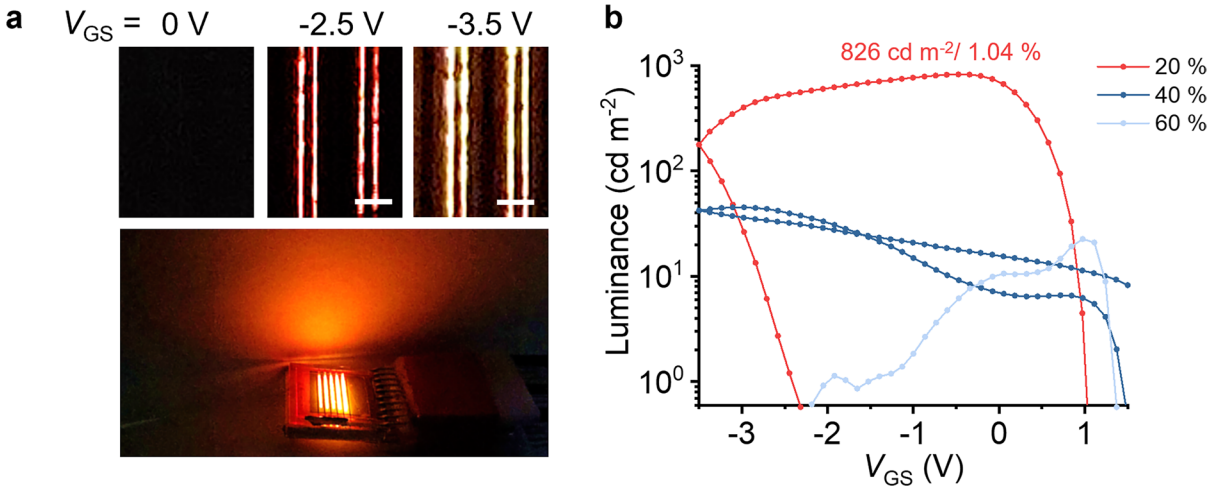

Extended Data Fig. 6 | Enhanced light-emission performance enabled by TBA-BF4 incorporation. (**a**) Images of the EOLET devices showing a clear and spatially PRZ with a light emission width of 247 µm after incorporating the ionic additive TBA-BF_4. Bar: 1 mm (**b**) Luminance characteristics as a function of V_{GS}, demonstrating a significantly improved maximum luminance of 826 cd m^{-2} and an external quantum efficiency of 1.04%. The enhanced luminance and EQE originate from improved charge injection induced by uncompensated ionic charge accumulation near the electrodes, while the PRZ is preserved.

https://doi.org/10.1038/s41563-026-02613-7

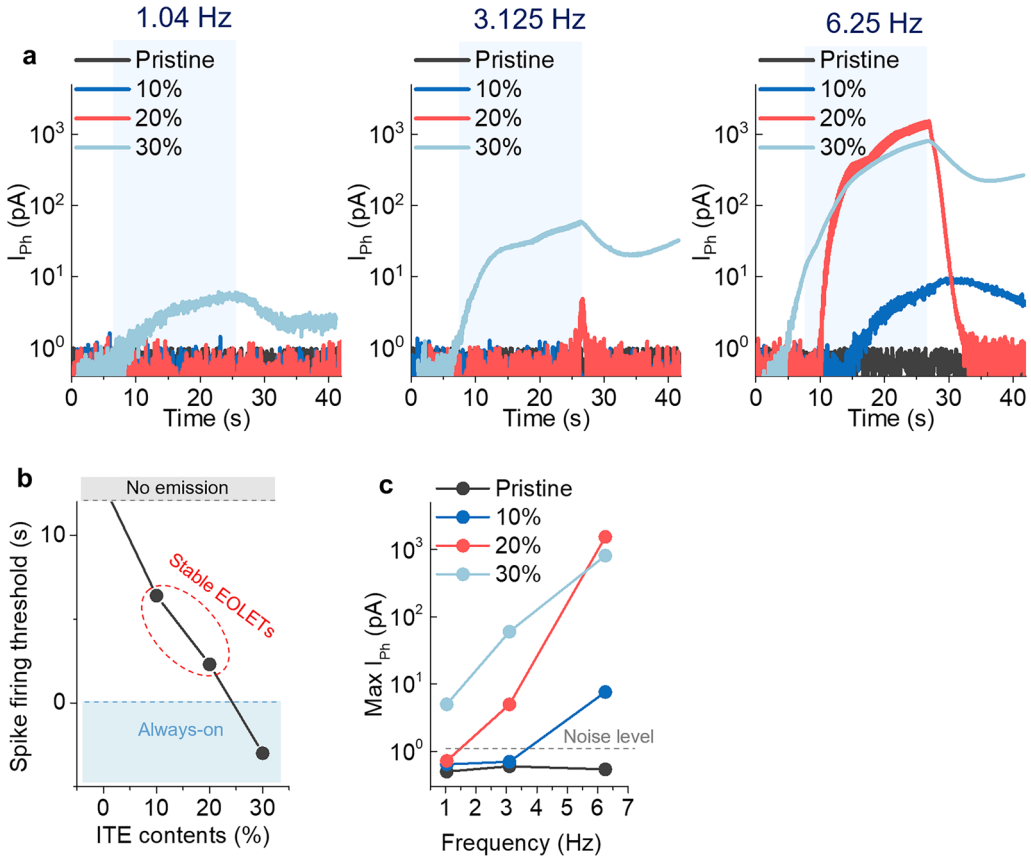

Extended Data Fig. 7 | Visual spike responses and threshold functions of EOLET. (**a**) Visual spike responses of flexible EOLET according to the input spike frequencies with the same voltage and duration conditions. ($V_{GS} = V_{DS} = -3.5$ V) (**b**) Spike-firing thresholds vs ITE content at 6.25 Hz. The EOLET with pristine LEP did not show visual spike responses because electron injection is very weak in unipolar electrolyte-gated OSTs as confirmed in Fig.3. As ITE content increased, the EOLET with 10% and 20% ITE-LEP showed spike firing thresholds of 6.4 s and 2.3 s, respectively, and the EOLET with 30% ITE-LEP showed an always-on state due to excess ITE. This trend aligns well with the analysis presented in Fig. 3. (**c**) Maximum I_{Ph} vs frequency of input spikes according to ITE content. Consistent with the above results, EOLET showed the same trend of increasing maximum I_{Ph} at all frequencies as ITE content increased. EOLETs that had ITE = 0, 10, or 20% exhibited spike-frequency-dependent plasticity, with maximum I_{Ph} increasing with frequency; the EOLET with ITE = 30% was permanently ON. In addition, an increase in ITE content led to a gradual decrease in the spike-firing frequency above the noise level. This controllable synaptic plasticity with visual outputs can be a core technique for emulating the versatile spike-processing capability in biological nerve.